n-Type Si solar cells with passivating electron contact: Identifying sources for efficiency limitations by wafer thickness and resistivity variation

Armin Richter[a],[*], Jan Benick[a], Frank Feldmann[a],[b], Andreas Fell[a], Martin Hermle[a], Stefan W. Glunz[a],[b]

[a] Fraunhofer Institute for Solar Energy Systems (ISE), Heidenhofstrasse 2, 79110 Freiburg, Germany
[b] Department of Sustainable Systems Engineering, Albert Ludwig University of Freiburg, Georges-Köhler-Allee 103, D-79110 Freiburg, Germany

ARTICLE INFO

ABSTRACT

In this work, the efficiency of *n*-type silicon solar cells with a front side boron-doped emitter and a full-area tunnel oxide passivating electron contact was studied experimentally as a function of wafer thickness W and resistivity ρ_b. Conversion efficiencies in the range of 25.0% have been obtained for all variations studied in this work, which cover 150 μm to 400 μm thick wafers and resistivities from 1 Ω cm to 10 Ω cm. We present a detailed cell analysis based on three-dimensional full-area device simulations using the solar cell simulation tool Quokka. We show that the experimental variation of the wafer thickness and resistivity at device level in combination with a detailed simulation study allows the identification of recombination induced loss mechanisms. This is possible because different recombination mechanisms can have a very specific influence on the *I-V* parameters as a function of W and ρ_b. In fact, we identified Shockley-Read-Hall recombination in the c-Si bulk as the source of a significant *FF* reduction in case of high resistivity Si. This shows that cells made of high resistivity Si are very sensitive to even a weak lifetime limitation in the c-Si bulk. Applying low resistivity 1 Ω cm *n*-type Si in combination with optimized fabrication processes, we achieved confirmed efficiency values of 25.7%, with a V_{OC} of 725 mV, a *FF* of 83.3% and a J_{SC} of 42.5 mA/cm^2. This represents the highest efficiency reported for both-sides contacted c-Si solar cells. Thus, the results presented in this work demonstrate not only the potential of the cell structure, but also that a variation of the wafer thickness and resistivity at device level can provide deep insights into the cell performance.

1. Introduction

Carrier-selective passivating contacts have been one of the key enabling technologies for the recent tremendous efficiency improvements within the field of crystalline silicon (c-Si) solar cells [1–8]. Among the different passivating contact approaches [9,10] (and reference therein), the most well-known example is the heterojunction of hydrogenated amorphous silicon and crystalline silicon (a-Si:H/c-Si). The application of this structure allows open-circuit voltages, V_{OC}, up to 750 mV [11] due to an extremely low surface recombination. The realization of an IBC cell featuring the a-Si/c-Si heterojunction led to an efficiency of 26.6% [8], an outstanding value less than 3%$_{abs}$ below the theoretical limit of 29.4% [12].

Another passivating contact approach is based on a stack of a high-quality ultra-thin SiO$_x$ layer which is capped by a heavily doped Si thin film and subsequently annealed (e.g. poly-Si [13,14], SIPOS [15,16], TOPCon [4]). Compared to a-Si:H, these approaches have a consider-

ably improved tolerance to high-temperature back-end metallization processes like screen printing and firing [17,18]. This approach benefits from the excellent surface passivation properties realized with the ultra-thin SiO$_x$ layer, while maintaining at the same time excellent contact resistance properties, as demonstrated by several research groups [4,14,19–21].

In our approach we combine the advantages of tunnel oxide passivating contacts (TOPCon) with those of a classical homojunction with its excellent electrical properties and optical transparency. This is realized by using TOPCon as a full-area electron contact on the rear surface of an *n*-type c-Si solar cell with a boron-doped front side emitter [4,5,22], as shown in Fig. 1. The excellent electrical and optical properties of the boron-doped emitter are based on an Al$_2$O$_3$ surface passivation [23–25]. The full-area rear contact allows not only high V_{OC} values due to the excellent passivation properties, but also very high fill factors *FF*, as there is no lateral current flow contribution for the electrons within the silicon bulk [5,26]. So far, efficiencies up to 25.1%
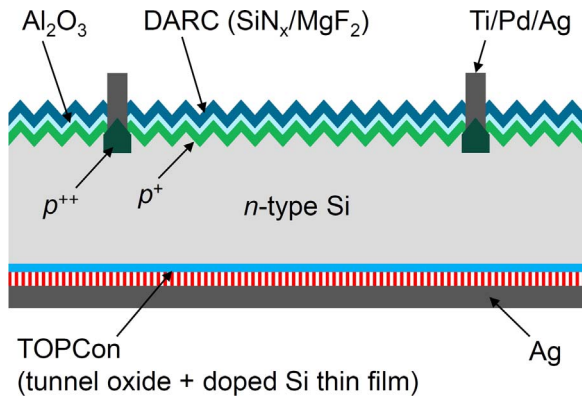
Fig. 1. Schematic cross-section of the *n*-type Si solar cell with diffused front boron-doped emitter and full-area passivating rear contact (TOPCon).

featuring *FFs* > 83% have been achieved with this cell structure [5].

In this work, we studied the efficiency of these cells experimentally as a function of wafer thickness *W* and resistivity ρ_b (i.e. the base doping) on a 25% efficiency level. Based on a detailed cell analysis using three-dimensional (3D) full-area device simulation together with experimentally determined input parameters, we are able to identify and quantify the main loss mechanisms of this cell structure and to estimate the efficiency potential of the structure.

2. Experimental

The TOPCon solar cells fabricated within this study have a designated area of 2×2 cm^2 and were made of high-quality (100)-oriented *n*-type float-zone (FZ) Si wafers with a diameter of 100 mm. Wafers with three different resistivities (1 Ω cm, 5 Ω cm and 10 Ω cm) and a thickness[1] of 200 μm were used for the resistivity variation and wafers with three different thicknesses (150 μm, 200 μm and 400 μm) and a resistivity of 5 Ω cm were used for the thickness variation.

The front side of the solar cells features an alkaline textured (random-pyramids) surface with a boron-doped *p*$^+$ emitter. The emitter was formed by BBr$_3$ tube furnace diffusion at 870 °C followed by drive-in oxidation, resulting in an emitter with a sheet resistance of $R_{sheet,p+} = 300$ Ω/sq. The emitter was passivated with a 10 nm thick Al$_2$O$_3$ layer deposited with plasma-assisted atomic layer deposition [25]. The front side was additionally coated with a double-layer antireflection coating (DARC) consisting of 50 nm SiN$_x$ grown by plasma-enhanced chemical vapor deposition (PECVD) and 90 nm thermally evaporated MgF$_2$.[2] Prior to the MgF$_2$ deposition, contact openings were etched wet-chemically through the front side Al$_2$O$_3$/SiN$_x$ coating and the front side metal contacts were formed with a stack of e-beam evaporated Ti/Pd/Ag (833 μm pitch). To reduce surface recombination losses at the front metal contacts, a heavily doped *p*$^{++}$ emitter is located underneath the contacts, also diffused in a BBr$_3$ tube furnace process and a subsequent drive-in. All structuring processes required for the front side are based on photolithography (partially to structure thermally-grown SiO$_2$ mask layers) and the lift-off technique. The full-area TOPCon electron contact on the rear surface is formed by an ultra-thin wet-chemical (HNO$_3$-based) SiO$_x$ layer covered by a 15 nm thick phosphorous-doped Si compound layer deposited with PECVD, which is annealed afterwards in a tube furnace at 800 °C (process details in Ref. [4,27]). The rear side metallization is realized by thermally evaporated

Ag.

The 1-sun current-voltage (*I-V*) parameters of the solar cells were measured under standard testing conditions (STC: AM1.5g, 100 mW/cm^2, 25 °C) using a sun-simulator with an incident current calibration based on certified *I-V* measurements (Fraunhofer ISE CalLab) for each wafer thickness. The pseudo fill factor *PFF* as well as *effective minority carrier lifetime* τ_{eff} of the finished solar cells were extracted from illumination intensity vs. V_{OC} (Suns-V_{OC}) measurements [28,29] using the Suns-V_{OC} setup from Sinton Instruments. The total series resistance of the cells under illumination conditions, $R_{s,light}$, was determined from the voltage difference of the Suns-V_{OC} and the 1-sun *I-V* data at maximum power point (mpp) [30,31]. The parallel resistance R_p was extracted from the slope of the *I-V* characteristic measured in the dark, using a linear fit in a voltage range of 300 ± 60 mV.

3. Simulation setup

3D device simulations of the fabricated solar cells were performed with Quokka [32,33], a solar cell simulation tool based on the conductive boundary approach [34] in which the surfaces are defined with recombination parameters, J_0, and sheet resistances, R_{sheet}. Full-area 3D simulations were conducted for a quarter of the solar cell including the dark perimeter (cf. Fig. 2), in order to account also for cell edge losses of these small area solar cells embedded in a wafer. All simulation input parameters (listed in Table A1) were determined experimentally, e.g. based on τ_{eff} measurements at symmetrically processed lifetime samples (with Al$_2$O$_3$-passivated *p*$^+$ emitter or TOPCon on *n*-type Si) for the J_0 values, or with four point probe measurements for the R_{sheet} values. The optical model is based on lumped parameters, i.e. a wavelength-dependent front surface trans-mission and a parameterization of the pathlength enhancement *Z*, which is independent of *W*. The parameters were extracted from the measured reflectance and *EQE* data shown in Fig. 6, as described in Ref. [35]. Notably, the determined *Z* parameters accurately describe the *EQE* curves for all wafer thicknesses. For some simulations, Shockley-Read-Hall (SRH) recombination [36,37] within the c-Si bulk was considered using the recombination properties of interstitial Fe [38]. All details of the simulation setup are described in the Appendix A.

4. Results and discussion

4.1. Solar cell results

The measured *I-V* parameters and *PFF* of the cells are shown in Fig. 3 for the resistivity variation and in Fig. 5 for the thickness variation. The box plots summarize the results of 10–12 cells per group except for the cells made of 150 μm thick 5 Ω cm material, of which only 6 cells were fabricated. The graphs show also simulation results which are discussed in Section 4.2. The *I-V* parameters of the best cells per variation are compared in Table 1, showing that efficiency values in the range of 25% were obtained for all variations. For two variations, the 200 μm thick 1 Ω cm base as well as the 400 μm thick 5 Ω cm base, independently confirmed efficiency values up to 25.3% were achieved.

A closer look at the resistivity, ρ_b, variation shown in Fig. 3 reveals a slight reduction of the efficiency with increasing ρ_b, from a peak value of 25.3% for 1 Ω cm wafers to 25.0% for 10 Ω cm wafers. The J_{SC} is independent of ρ_b at a very high level of about 42.5 mA/cm^2. The V_{OC} shows a slight increase with increasing ρ_b, on average from 716 mV for 1 Ω cm to 718 mV for 10 Ω cm. This weak effect is, however, over-compensated by a pronounced *FF* reduction of about 0.7%$_{abs}$ with increasing ρ_b, on average from a high level of around 82.5 to a level around 81.8%. The same reduction is also observed for the *PFF* values on a ~2.5%$_{abs}$ higher level. Due to some scattering, which is discussed below, this reduction can be best observed from the peak values. Unlike *FF*, the *PFF* values extracted from the Suns-V_{OC} measurements are not influenced by series resistances [29]. Thus, the observed trends of *PFF*

---

[1] For simplicity, the nominal thick is used throughout the text to refer to the different materials although the measured thickness is ~3 μm thinner than the nominal thickness except the 400 μm thick material, which is ~3 μm thicker. For the calculations and simulations, however, the measured thickness values were used.

[2] These layer thicknesses are nominal values, which are in good agreement with the thicknesses measured perpendicular to the faces of the random pyramids using SEM images.
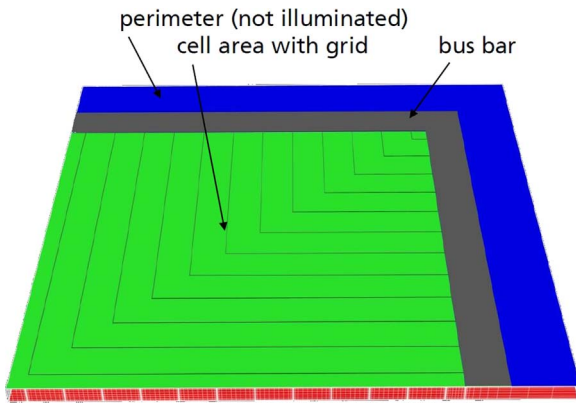
Fig. 2. Quarter of the fabricated solar cell (i.e. 1×1 cm^2 active area) including busbar (located outside the active area) and the dark perimeter, as simulated in 3D with Quokka.

and *FF* are a strong indication that the obtained *FF* reduction is *not* induced by an increased series resistance due to the higher base resistivity. This is supported by the $R_{s,light}$ data shown in Fig. 4a. Although there is some scattering in the $R_{s,light}$ data (in particular for the 5 Ω cm material), very similar $R_{s,light}$ values around 0.4 Ω cm^2 can be observed for the 1 Ω cm and the 10 Ω cm material. Thus, for these 25% efficient *n*-type Si cells, it is experimentally evident that an increase of the base resistivity from 1 Ω cm to 10 Ω cm does not increase the series resistance of the cells. However, the decrease in *PFF* leads to a significant *FF* loss. The reason for this *FF*, i.e. *PFF*, reduction is analyzed in Section 4.2.

The *I-V* results of the wafer thickness variation shown in Fig. 5 reveal that the efficiency increases with increasing wafer thickness, *W*, from a peak value of 24.9% for the 150 μm thick cells to 25.3% for the 400 μm thick cells. At the same time, V_{OC} decreases from a level around 720 mV to around 712 mV, respectively. Such a decrease in V_{OC} is actually expected as the recombination within the silicon bulk increases with *W*. The average *FF* is on a rather constant level around 81.5%, while the peak *FF* values show a weak increase with increasing *W*. The observed efficiency increase with increasing thickness is, however, dominated by the strong increase in J_{SC} from 42.2 mA/cm^2 for the 150 μm thick cells to over 43.0 mA/cm^2 for the 400 μm thick cells, with a peak value of 43.3 mA/cm^2 (cf. Table 1), which represents the highest J_{SC} reported so far for single junction c-Si solar cells. These high short circuit currents were independently confirmed by Fraunhofer ISE CalLab and National Renewable Energy Laboratory (NREL) within an average deviation of $\leq 0.7\%$. The increasing J_{SC} with increasing *W* results from a more effective absorption of the weakly absorbed long wavelength light ($\lambda > 1000$ nm) as the mean pathlength of this light inside the cell scales with *W* [35]. This improved IR response can be clearly observed from the *EQE* and *IQE* data shown in Fig. 6 measured on representative cells of each thickness. At $\lambda > 1000$ nm, the *EQE* increases with *W* while *R* (i.e. the escaping light) decreases due to the more effective absorption. With respect to the *FF* it can be observed that the *PFF* increase is more pronounced than the *FF* increase, which indicates that the series resistance of the cells increases with increasing *W*. This is quantified by the respective $R_{s,light}$ data shown in Fig. 4b, as $R_{s,light}$ slightly increases from an average level of 0.4 Ω cm^2 for *W* = 150 μm to 0.5 Ω cm^2 for *W* = 400 μm. Thus, the strong increase in *PFF* with increasing *W* is partially compensated by an increasing series resistance.

In order to identify the influence of shunts on the observed *PFF* trends and hence, on the *FF* trends, the parallel resistance R_p of the cells was extracted from *I-V* data measured in the dark. The respective R_p data is shown in Fig. 7. As can be seen, R_p shows neither a systematic trend as function of *W* nor as a function of ρ_b. On average, R_p is at a level of around 3.5 kΩ cm^2 for all variations, with a scattering from ~2 kΩ cm^2 to ~6 kΩ cm^2. Hence, the observed parallel resistances

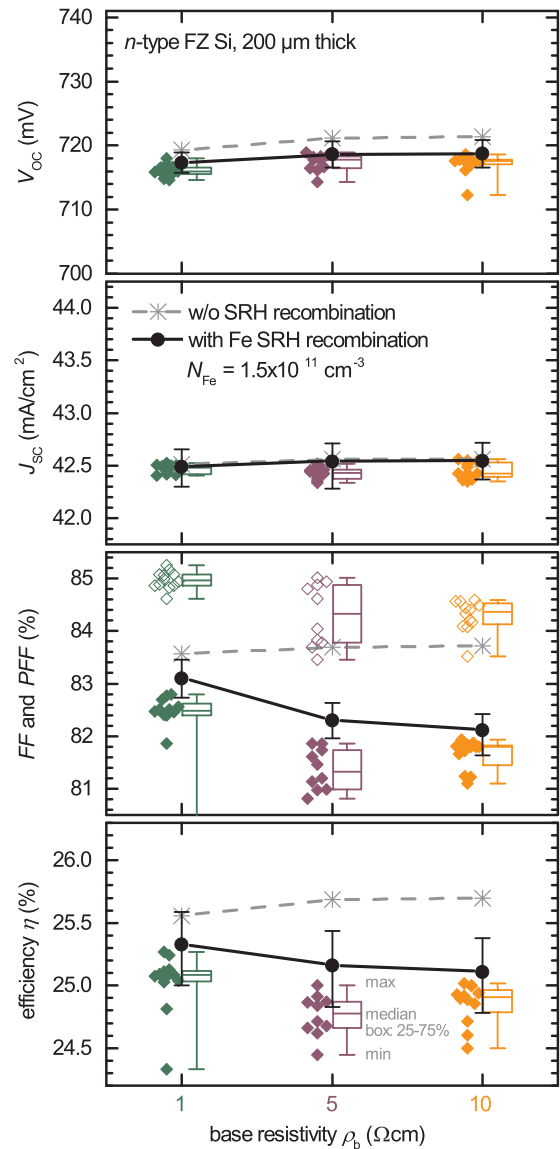**Fig. 3.** Box plot of the *I-V* parameters and *PFF* (open symbols) of the 200 μm thick solar cells as a function of the base resistivity. The experimental data is compared to 3D device simulation results shown as well (lines are guides-to-the-eyes). The simulations were performed using Quokka for a quarter of the total cell including the dark perimeter. The simulation results are shown for two different simulation configurations: with (black symbols) and without (grey symbols) SRH recombination in the c-Si bulk. Note that simulation results are not shown for *PFF*. The scale range of the V_{OC}, J_{SC} and *FF* graphs represent the same relative effect on η. The error bars represent exemplarily the uncertainty of the simulation results with Fe SRH recombination according to the uncertainties of the input parameters given in Table A1.

Table 1
I-V parameters as well as *PFF*, $R_{s,light}$ and R_p of the best cells per variation. All cells have an area of 2×2 cm^2 (designated area) and were measured under STC.

ρ_b (Ω cm)	W (μm)	V_{OC} (mV)	J_{SC} (mA/cm^2)	FF (%)	PFF (%)	η (%)	$R_{s,light}$ (Ω cm^2)	R_p (kΩ cm^2)
1	200	718.0	42.5	82.8	85.2	25.3[a]	0.38	3.6
5	150	720.4	42.2	81.7	84.3	24.9	0.38	2.7
5	200	718.9	42.5	81.9	84.6	25.0	0.44	3.9
5	400	712.5	43.3	81.9	85.3	25.3[a]	0.52	3.5
10	200	717.8	42.5	81.9	84.6	25.0[a]	0.43	5.2

[a] independently confirmed by Fraunhofer ISE CalLab.

provoke a certain *FF* reduction and the scattering of R_p contributes strongly to the scattering of *FF* and *PFF*, but it does not explain any systematic trend of the *FF* and *PFF*, neither for the thickness variation
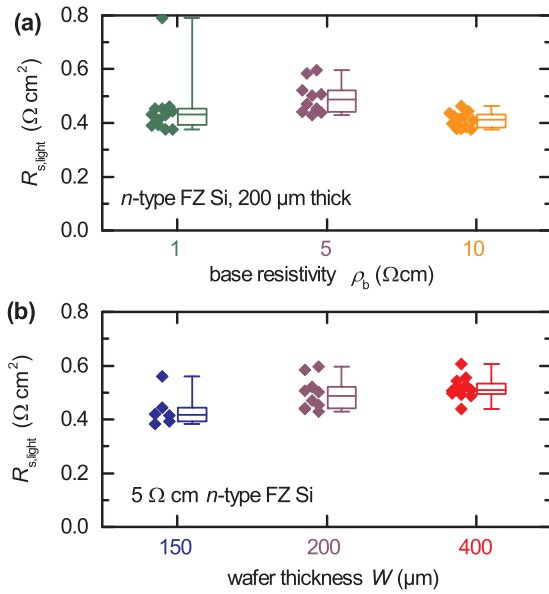
Fig. 4. Total series resistance of the cells under illumination conditions, $R_{s,light}$, as determined from the Suns-V_{OC} and the 1-sun I-V data. (a) shows $R_{s,light}$ for the base resistivity variation and (b) for the thickness variation.

nor for the resistivity variation. These relatively low R_p values are attributed to the busbar located outside the active cell area (cf. Fig. 2), but it is not related to the cell structure as shown in Fig. 1.

The results described above revealed significant trends of the I-V parameters as a function of the wafer thickness and resistivity. However, the decreasing efficiency with increasing resistivity was, for instance, not expected as rather ρ_b-independent efficiencies have been predicted in previous studies, at least for $\rho_b > \sim 1 \, \Omega$ cm material of high quality, i.e. low bulk defect recombination [5,26]. The observed efficiency reduction was found to correlate with a PFF reduction but not with the series resistance $R_{s,light}$. Thus, the PFF plays an important role for the interpretation of the cell results. A similar important role of PFF was also observed for the thickness variation. In both cases, a dominating role of shunts can be excluded. The PFF is, however, not only sensitive to shunts, but also to charge carrier recombination properties, either within the silicon bulk, the junction or at the surface [29]. Therefore, the observed PFF trends and hence, the FF trends are most likely strongly induced by these recombination effects. Such recombination induced effects on FF were reported, for instance, for impurity recombination within the silicon bulk [26,39] or for injection-dependent surface recombination [3,40]. Recombination in the (dark) perimeter is another significant efficiency loss for the small area solar cells embedded in a wafer, which is – at least to some extent – due to a FF reduction [41,42].

4.2. Simulation results

In order to identify the nature of the dominating recombination mechanisms, we performed device simulations as described in Section 3. For these simulations, we considered perimeter recombination losses as well as surface recombination properties, based on experimentally determined, injection-independent J_0 values (cf. Appendix A). The simulation results are shown in Figs. 3 and 5 (results without SRH recombination). The simulated J_{SC} is in good agreement with the measured values in particular for the W-variation, which shows that the lumped optical parameters describe the optics of the cells pretty well. With an offset of about 3 mV, the simulated V_{OC} is already very close to the measured values. The simulated FF, however, is at an almost ρ_b-independent and W-independent level around 83.6%, which is significantly higher than the experimental results. This FF disagree-
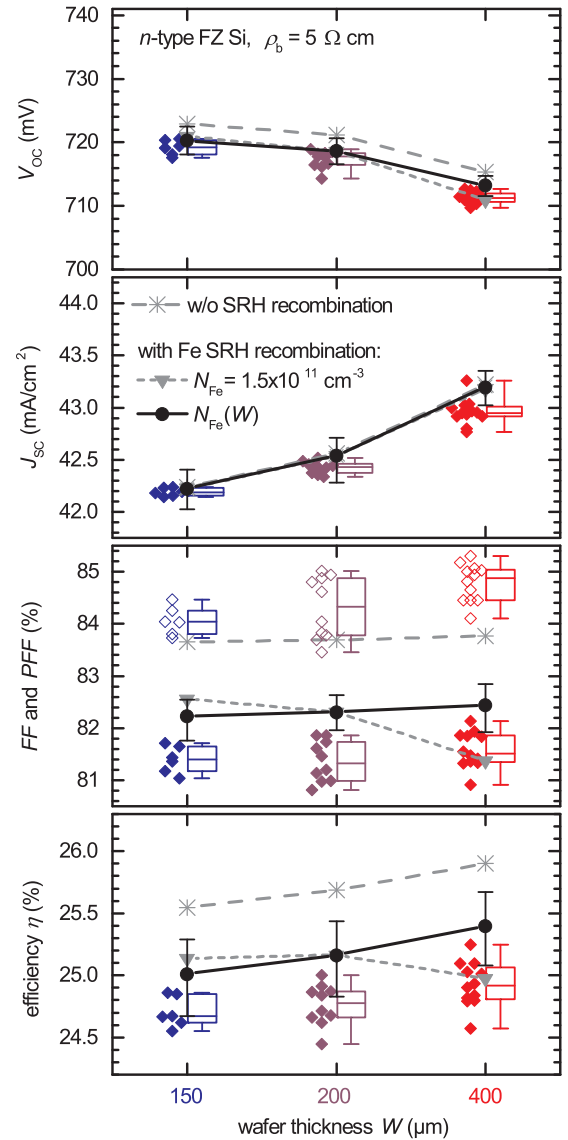

Fig. 5. Box plot of the I-V parameters and PFF (open symbols) as a function of the wafer thickness (5 Ω cm n-type FZ Si). The data is presented analogously to Fig. 3. The simulation results are shown for one additional SRH recombination assumption: $N_{Fe}(W)$ according to Eq. (1) with $D_{Fe} = 3 \times 10^9$ cm^{-2}, which results in $N_{Fe}(200 \, \mu m) = 1.5 \times 10^{11}$ cm^{-3} as assumed for the W-independent N_{Fe}.

ment results in an analogous disagreement of the simulated and measured efficiency.

Non-ideal, injection-dependent surface recombination or SRH recombination in the c-Si bulk induced by impurity contamination are possible sources for additional FF losses. Although injection-independent J_0 values were not observed experimentally at the symmetrically processed lifetime samples (cf. Fig. A1), indicating ideal surface recombination, the solar cells might still suffer from injection-dependent, non-ideal surface recombination as considerably more process steps are involved in the solar cell fabrication (e.g. the photolithography processes). With respect to SRH recombination, it is important to emphasize that the recombination properties of the high-quality FZ wafers used for the solar cells were tested prior to the solar cell fabrication using symmetrically passivated lifetime samples. The τ_{eff} level measured at these samples was very close to the intrinsic lifetime limit as observed in Ref. [43], for which reason the initial impurity concentration can be considered to be insignificant. However, our lab-type high-efficiency cell fabrication sequence contains several high temperature processes above ~900 °C, e.g. the thermal growth of
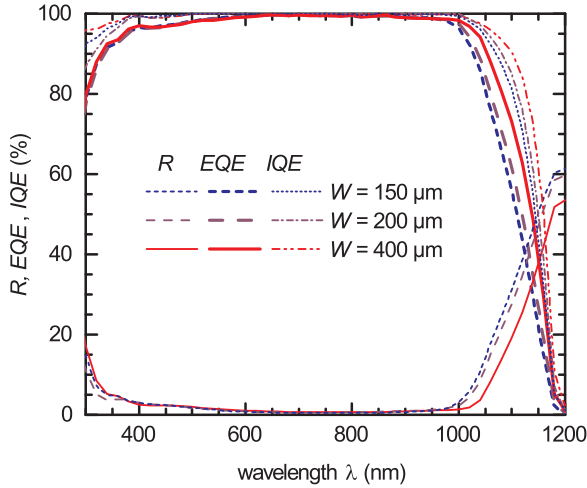
Fig. 6. Measured external quantum efficiency *EQE*, reflectance *R* and the internal quantum efficiency *IQE* of characteristic cells featuring the three different wafer thicknesses studied in this work.
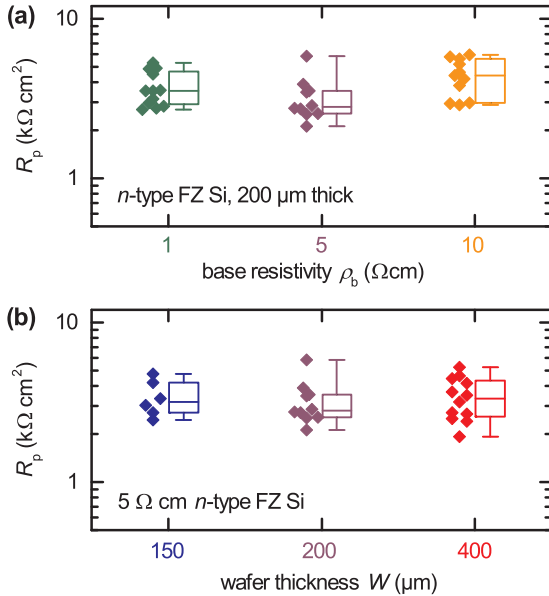

Fig. 7. Parallel (shunt) resistance R_p extracted from the slope of the dark *I-V* curves around 300 mV. (a) shows R_p for the ρ_b variation and (b) for the *W* variation.

masking SiO_2 layers or the drive-in diffusion of the p^+ emitter. All of these processes bear the risk of introducing impurities into the c-Si bulk, in particular transition metals such as Cr, Fe, Co, Ni, Cu and Au, which are well known for their recombination activity in c-Si [44–46] and which are also highly mobile in c-Si at these high temperatures.[3]

In order to find out whether non-ideal recombination at the surface or SRH recombination within the silicon bulk or even a combination of both are the origin of the additional *FF* reduction, we performed device simulations considering exemplarily interstitial Fe as SRH recombination center within the c-Si bulk. A recombination parameter J_{02} with an ideality factor of $n = 2$ was considered to account for non-ideal, injection-dependent surface recombination exemplarily for the Al_2O_3-passivated p^+ emitter at the front surface, which is referred to as $J_{02,p+}$. The device simulations were performed with the setup as described in Section 3, however, for the sake of computing time, a two-dimensional

---

[3] For instance, Cr, Fe, Co, Ni, Cu and Au have a very high diffusivity in c-Si [44,45,47], which is more than 8 orders of magnitude higher than, for instance, the diffusivity of B in c-Si. Due to this high diffusivity, these impurities diffuse > 200 μm already after 30 min at 900 °C [45,48].

(2D) unit cell of the solar cell structure shown in Fig. 1 was applied.

Fig. 8 shows the simulation results as a function of $J_{02,p+}$ for different Fe concentrations, N_{Fe}: in (a) the efficiency exemplarily for the 200 μm thick 5 Ω cm material and in (b) the *FF* difference for the wafer thickness variation, $\Delta FF_{sim}(W) = FF_{sim}(400\ \mu m) - FF_{sim}(200\ \mu m)$, and the resistivity variation, $\Delta FF_{sim}(\rho_b) = FF_{sim}(10\ \Omega\ cm) - FF_{sim}(1\ \Omega\ cm)$, which is compared to the respective experimentally obtained differences $\Delta FF_{exp}(W)$ and $\Delta FF_{exp}(\rho_b)$ (horizontal lines in Fig. 8b). If only $J_{02,p+}$ is considered, the simulation results indicate a good agreement with the measured results of thickness variation for a $J_{02,p+}$ around 4 nA/cm². At this $J_{02,p+}$, however, the simulated results do not agree with the measured results of the resistivity variation, as $\Delta FF_{sim}(\rho_b)$ is almost zero. If only SRH recombination is considered (see Fig. 9), a reasonable agreement of simulated and measured results can be obtained for the ρ_b variation with $N_{Fe} \approx 1.5 \times 10^{11}\ cm^{-3}$, which describes the $\Delta FF_{sim}(\rho_b)$ very well. However, the *FF* reduction is even more pronounced for the *W* variation, which is again in disagreement with the measured results, as $\Delta FF_{exp}(W)$ is almost zero or even slightly positive. These trends are modified to some extent, if SRH recombination is combined with $J_{02,p+}$ (see Fig. 8). However, a reasonable agreement of simulated and measured values is not observed for any combination. Thus, neither $J_{02,p+}$ nor Fe SRH recombination or even a combination of both can describe the experimental results of the resistivity *and* the thickness variation consistently.

This changes remarkably, if the total amount of Fe impurities within the wafer is assumed to be constant instead of the constant impurity density N_{Fe} assumed so far. This might be actually a very realistic scenario, if the impurities are introduced into the silicon bulk via a surface contamination and a subsequent in-diffusion during high temperature processes. In this case, the impurity concentration scales inversely with the wafer thickness and can be described with an area dose D_{Fe}:

$$N_{Fe}(W) = D_{Fe}W^{-1}. \tag{1}$$

Under this assumption (without assuming an additional $J_{02,p+}$), the simulation results for the ρ_b variation are not affected, as $W = const.$, but the results for the *W* variation are significantly altered. This is shown in Fig. 9 as a function of $N_{Fe}(W = 200\ \mu m)$. The *FF* now tends to increase slightly with *W*, as observed experimentally, and there is a D_{Fe} ($= 3 \times 10^9\ cm^{-2}$, i.e. $N_{Fe}(W = 200\ \mu m) = 1.5 \times 10^{11}\ cm^{-2}$) for which these 2D device simulation results indicate a good agreement with the experimental values of the resistivity *and* the thickness variation, i.e. a consistent description for both variations.

This agreement was verified with the 3D full area simulations including perimeter. The results of these simulations are compared to experimental data in Figs. 3 and 5. As can be seen, there is a good agreement of the simulated and measured values for all *I-V* parameters. For the *W* variation, Fig. 5 compares also simulations results obtained for the $N_{Fe}(W)$ assumption with those of the constant N_{Fe} assumption. It can be clearly seen that a constant N_{Fe} results in a decreasing *FF* with increasing *W*, which is in disagreement with the experimental data.

Fig. 10 illustrates the influence of the constant N_{Fe} and $N_{Fe}(W)$, i.e. constant D_{Fe}, assumption on the effective lifetime τ_{eff}. The graph shows $\tau_{eff}(\Delta n)$ data measured on the best cell of each variation together with calculated $\tau_{eff}(\Delta n)$ data (as described in the Appendix B). With respect to SRH recombination, the three scenarios were considered: (i) without SRH recombination, (ii) with constant impurity concentration ($N_{Fe} = 1.5 \times 10^{11}\ cm^{-3}$) and (iii) with $N_{Fe}(W)$ according to Eq. (1) and $D_{Fe} = 3 \times 10^9\ cm^{-2}$. Scenario (i) clearly overestimates τ_{eff} considerably around mpp. In scenario (ii), the SRH lifetime is at $\tau_{SRH} = 8.9$ ms independent of ρ_b and *W*, and for Fe actually also independent of Δn. With this τ_{SRH} limitation, the discrepancy between measured and calculated τ_{eff} clearly vanishes for the resistivity variation, but it underestimates τ_{eff} of the 400 μm thick cell significantly. With scenario (iii), the discrepancy in τ_{eff} at mpp vanishes also for the thickness variation and all measured lifetime curves can be reproduced.
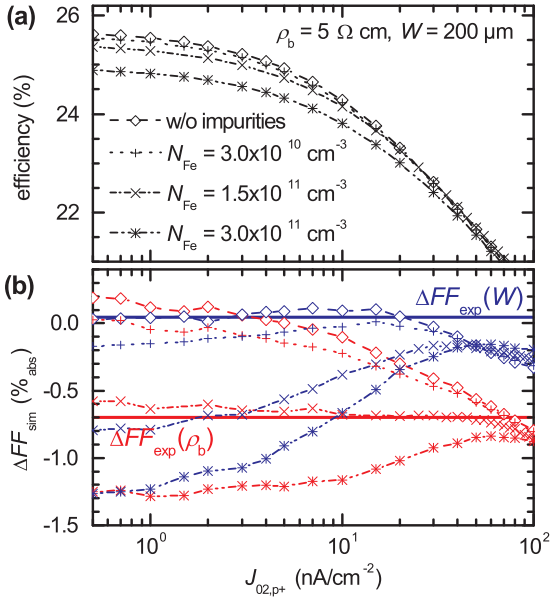
Fig. 8. (a) shows the simulated efficiency as a function of the recombination parameter $J_{02,p+}$ exemplarily for the 200 μm thick 5 Ω cm material with and without Fe SRH bulk recombination for three representative Fe concentrations. (b) shows the simulated FF differences for the W-variation ($\Delta FF_{sim}(W)$ in blue) and ρ_b-variation ($\Delta FF_{sim}(\rho_b)$ in red). The horizontal lines for $\Delta FF_{exp}(W)$ and $\Delta FF_{exp}(\rho_b)$ represent the corresponding differences observed experimentally. The device simulations were performed with Quokka for a 2D unit cell, as described in the text.
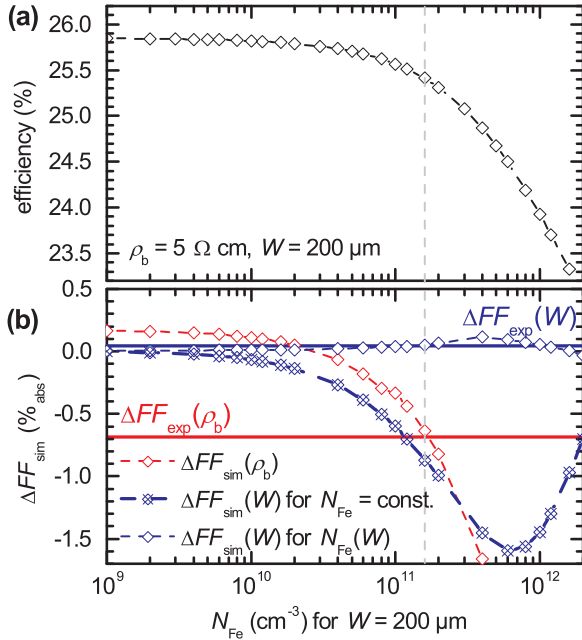

Fig. 9. (a) shows the simulated efficiency as a function of Fe concentration N_{Fe} exemplarily for the 200 μm thick 5 Ω cm material (without a $J_{02,p+}$ contribution). (b) shows the simulated FF differences for the W-variation ($\Delta FF_{sim}(W)$ in blue) and ρ_b-variation ($\Delta FF_{sim}(\rho_b)$ in red) analogously to Fig. 8. For the W variation, simulations results are show for a W-independent N_{Fe} as well as for $N_{Fe}(W)$ according to Eq. (1). Note that these both N_{Fe} assumptions result in the same N_{Fe} for the ρ_b-variation (as W = const. = 200 μm).

At this point it is interesting to point out that the τ_{eff} at mpp of the 10 Ω cm solar cell is with 2.9 ms about twice the mpp τ_{eff} of the 1 Ω cm cell. This indicates less charge carrier recombination at mpp in the 10 Ω cm material, although the efficiency obtained for the 10 Ω cm material is lower than that for the 1 Ω cm material (cf. Table 1). The reason for this is the injection-dependent quasi-Fermi level position of
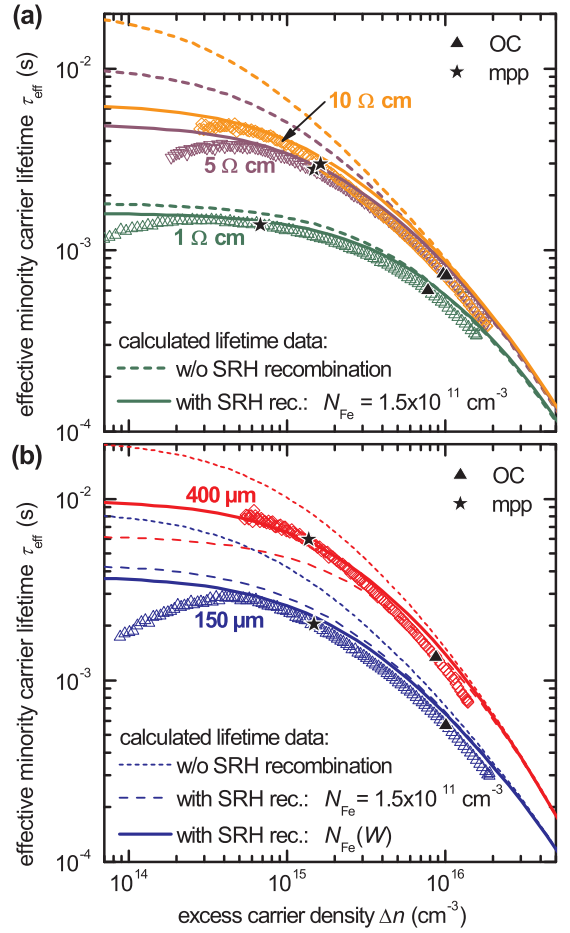

Fig. 10. Effective lifetime τ_{eff} (open symbols) as a function of Δn measured at the final solar cell (the cells listed in Table 1). τ_{eff} was extracted from Suns-V_{OC} measurements. (a) shows τ_{eff} for the resistivity variation (W = 200 μm) and (b) for 150 μm and 400 μm thick wafers (ρ_b = 5 Ω cm). The ▲ and ★-symbol represent τ_{eff} at open-circuit (OC) and maximum power point (mpp) condition, respectively. The experimental lifetime data are compared to calculated lifetime data with and without Fe SRH recombination as described in the text.

the majority charge carriers, whose contribution to the quasi-Fermi level splitting is more important in case of lowly doped silicon (i.e. high resistivity) as the equilibrium Fermi level is more distant from the band edge. To compensate this, a cell made of high resistivity Si needs to operate at a considerably higher Δn level and consequently, at a higher mpp τ_{eff}.

The results of the simulation study, as discussed so far, indicate clearly that a SRH recombination with a constant dose of impurities describes the experimental solar cell results consistently, rather than a constant impurity concentration or injection-dependent surface recombination (e.g. due to $J_{02,p+}$). In fact, the independent variation of ρ_b and W at the device level allowed to identify this impurity based loss mechanism due to its specific influence on the I-V parameters as a function of wafer thickness and resistivity. This ρ_b and W variation approach at device level can be considered as a combination of two approaches used to evaluate effective lifetime data of symmetrically processed lifetime samples: (i) the wafer thickness variation method, which is used for separating bulk and surface recombination properties [49], and (ii) the wafer doping variation method, which is used to characterize SRH recombination properties of impurities due to the sensitivity of SRH recombination on the doping concentration [50].

So far, we only considered Fe as SRH recombination center. In fact, we performed a comprehensive simulation study ($> 10^4$ device simulations) for various other transition metals well known for the recombination activity in Si, such as Ti, V, Cr, Ni, Cu, Zn or Au, which cover a wide range of energy levels and capture cross sections for electrons and

holes, and hence, a wide range of SRH recombination characteristics in c-Si. We found that for most of these elements rather similar conclusions can be drawn as discussed here exemplarily for Fe and even for a mixture of them, i.e. they can also provide a consistent description for the ρ_b and W variation when considered with the constant dose of impurities given in Eq. (1). Some other impurities (e.g. Cu and Au) can even be excluded due to their unique influence particularly on the *FF*. Therefore, we can conclude that these results strongly indicate that our cells suffer from a SRH recombination with a constant dose of impurities as described with Eq. (1). However, we *cannot* identify the impurity element(s), although a dominating role of some can be excluded. Details of this simulation study will be published elsewhere [51].

4.3. Efficiency potential

The 3D device simulations of a quarter of the cells including the perimeter and the $N_{Fe}(W)$ assumption according to Eq. (1) provide a quite accurate description of the cells fabricated in this work. Therefore, this cell model was used to quantify the power loss associated with the electrical loss mechanisms by applying the free energy loss analysis (FELA) approach [52], which is implemented in Quokka. The results are shown in Fig. 11 for the ρ_b and W variation. The results reveal that the main losses arise from recombination within the c-Si bulk, recombination at the p^+ emitter and due to the perimeter. With respect to bulk recombination, it is interesting that although the cells made of $1\,\Omega\,cm$ material suffer least from SRH recombination, the total bulk recombination losses are almost the same as for the 200 μm thick cells made of $\geq 5\,\Omega\,cm$ Si due to the considerably higher Auger recombination loss. The bulk recombination losses decrease with decreasing W due to a decrease of intrinsic recombination losses while at the same time the surface recombination losses increase, so that the total recombination losses are almost independent of W, which shows that with decreasing W these cells become more sensitive to surface recombination. The perimeter losses are almost independent of W and ρ_b, except for the $1\,\Omega\,cm$ material, which perimeter losses are a factor of 1.5 lower. Finally, it is important to point out that the power loss associated with the full-area passivating rear contact is rather small, e.g. the recombination losses are a factor 2.5 lower than that of the p^+ emitter, which demonstrates the potential of the TOPCon approach.

Based on this power loss analysis, the efficiency potential of the solar cell structure is expected to be > 25.5% for all materials and wafer thicknesses studied in this work, if recombination active impurities within the bulk can be avoided and a high parallel resistance can be achieved. Thus, although *n*-type wafers are considerably more tolerant to common impurities compared to *p*-type Si [46], this study underlines that on a very high efficiency level high base resistivity *n*-

Table 2
I-V parameters and *PFF* measured at the best cells of the second batch (made of 200 μm thick 1 Ω cm FZ Si, structure as shown in Fig. 1) under STC.

Area[b] (cm^2)	V_{OC} (mV)	J_{SC} (mA/cm^2)	FF (%)	PFF (%)	η (%)
4.0 (da)	724.9	42.5	83.3	85.7	25.7[a]
4.0 (ap)	727.6	42.2	83.2	86.2	25.6[a]

[a] Independently confirmed by Fraunhofer ISE CalLab.
[b] Designated area (da), aperture area (ap).

type Si wafers become sensitive even to slight bulk lifetime degradations induced by impurity recombination.

A second batch of solar cells has been fabricated basically as described in Section 2. In this batch, an improved front contact geometry was applied, which reduced the emitter recombination losses. Moreover, the TOPCon contact has been improved by replacing the HNO_3-based SiO_x growth process for an ozone-based oxidation process, which reduced the surface recombination. The cells were made of $1\,\Omega\,cm$ FZ Si (thickness of 200 μm) which was found to be less affected by SRH recombination losses. The *I-V* parameters are given in Table 2 for the best cell with a designated area of $2 \times 2\,cm^2$ (as described above) as well as with an aperture area of $2 \times 2\,cm^2$ (i.e. with busbar in the active cell area). A confirmed efficiency of 25.7% and 25.6% has been achieved, respectively. These values represent the highest efficiencies reported for *both-sides contacted* c-Si solar cells [53]. The cells benefit not only from a high V_{OC}, but also from a very high *PFF* level in the range of 86%, and consequently a high *FF* above 83%. These results demonstrate impressively the potential of the cell architecture studied in this work. A detailed analysis of these cells is in progress and will be published elsewhere.

5. Conclusions

In this work, the efficiency of *n*-type silicon solar cells with a front side boron-doped emitter and a full-area tunnel oxide passivating electron contact was studied experimentally as a function of wafer thickness W and resistivity ρ_b. Efficiency values in the range of 25% have been observed for all studied variations. An increase of the base resistivity was found to result in a significant *FF* and also *PFF* reduction; a trend which was not predicted in previous studies. To identify the origin of this behavior, a detailed device simulation study was performed with Quokka, taking non-ideal surface recombination and impurity recombination in the c-Si bulk into consideration. In fact, the very specific influence of the different recombination mechanisms on the *I-V* parameters as a function of W and ρ_b permitted the identification of impurity recombination in the c-Si bulk as a source for the *FF* loss.
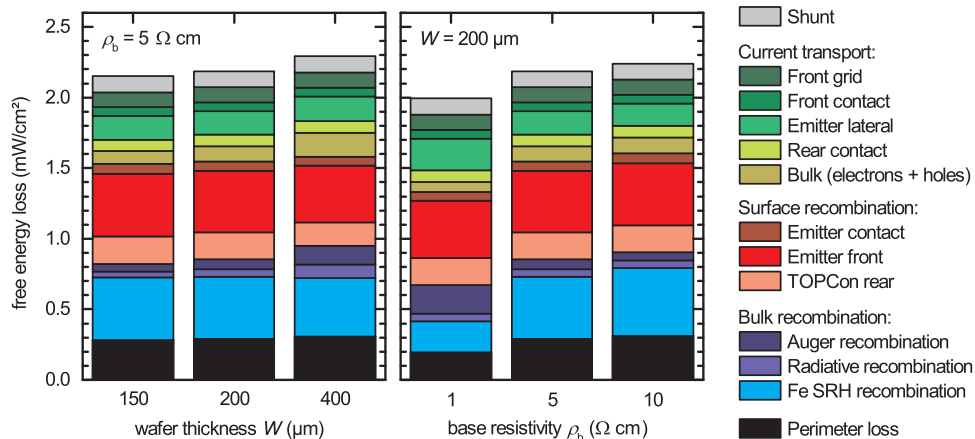

Fig. 11. Free energy loss analysis for the thickness and resistivity variation, based on the 3D Quokka simulations of a quarter of the cell including the perimeter, exemplarily for Fe impurities and $N_{Fe}(W)$ according to Eq. (1) with $D_{Fe} = 3 \times 10^9\,cm^{-2}$. Note that the power loss scale in mW/cm^2 is equivalent to an efficiency loss in %$_{abs}$.

The simulation results indicate also that the impurity concentration is a function of W and follows an area dose description, which suggest that the impurities are introduced over the surface during high temperature processes. Thus, the results presented in this work demonstrate not only the potential of the cell structure, but also that a variation of the wafer thickness and resistivity at device level can provide deep insights into the cell performance; a prerequisite for further device optimizations. The results show further that cells made of high resistivity Si are much more sensitive to lifetime limitations in the c-Si bulk, but the wafer resistivity has not a significant influence on the efficiency potential, mainly due to the one-dimensional electron transport in the base.

Finally, we presented cells fabricated with optimized processes. A peak efficiency of 25.7% has been achieved, which represents the highest efficiency reported for *both-sides contacted* c-Si solar cells as well as for c-Si solar cells with a *diffused junction*.

Appendix

A. Details of Quokka simulation setup

Quokka [32,33] was used to perform device simulations of the fabricated solar cells. 3D total area simulations were conducted for a quarter of the fabricated solar cells (i.e. 1×1 cm^2 active area) including the dark perimeter, as shown in Fig. 2, which represents a symmetry element of the whole cell. As can be seen, the busbar is located outside the active cell area on top the perimeter with an insulating stack between the busbar metal and silicon.[4] The rear perimeter area is covered with the same TOPCon/Ag stack as in the active cell area. A convergence analysis regarding the dark perimeter losses showed that a perimeter width of 2.5 mm underestimates this losses less than 10%$_{rel}$. Therefore, a width of 2.5 mm was considered, which also allows to solve the *I-V* parameters for this 3D quarter of the solar cell including perimeter (i.e. 1.25×1.25 cm^2) with more than 10^6 vertices in an reasonable time (less than days). The simulations were performed for standard testing conditions.

It is important to point out that all input parameters as specified in Table A1 were determined experimentally. The specific contact resistance to the front side p^{++} emitter was measured with the transfer length method (TLM) on dedicated contact structures. The grid finger line resistance was measured at dedicated finger structures. The optical model used to describe the solar cells is based on a lumped parameter approach, i.e. a front surface transmission T, calculated from the measured reflectance data excluding escape, and a pathlength enhancement Z, which was parameterized based on experimental *EQE* and *R* data as described in Ref. [35]. The resulting model fit parameters are also specified in Table A1.

In order to determine the surface passivation quality e.g. of the TOPCon rear contact and the front side p^+ emitter in terms of J_0, symmetrically processed lifetime samples were prepared together with the solar cells. The TOPCon lifetime samples were made of planar (100)-oriented n-type FZ Si wafers with the different resistivities used for the cells: 1 Ω cm, 5 Ω cm and 10 Ω cm and respective thicknesses of 200 µm, 150 µm and 200 µm. The p^+ lifetime sample was made of a (100)-oriented 10 Ω cm n-type FZ Si wafer with a thickness of 200 µm and alkaline textured surfaces, identical to the front surface of the cells. TOPCon as well as the Al$_2$O$_3$ passivated p^+ emitter were processed as described in Section 2. R_{sheet} of the p^+ emitter was measured with four point probe measurements, which is in good agreement with R_{sheet} extracted from the TLM measurements. The J_0 values were extracted from injection-dependent effective lifetime τ_{eff} data according to the high-injection method proposed by Kane and Swanson [54] applying the correction routines described by Kimmerle et al. [55]. τ_{eff} was measured with the photo-conductance decay (PCD) technique using the Sinton lifetime tester WCT120 in quasi-steady-state mode (QSSPC) [56] and the generalized analysis proposed by Nagel et al. [57]. The optical factor f_{opt} required for the QSSPC analysis was determined for each sample by adapting the QSSPC measurements to transient PCD measurements in an
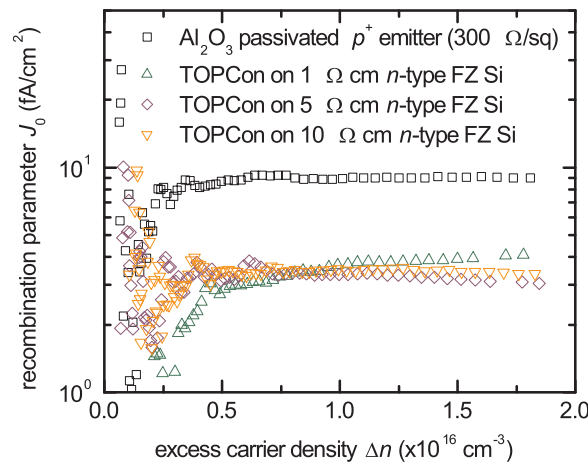

Fig. A1. Recombination parameter J_0 as a function of Δn for the Al$_2$O$_3$ passivated p^+ emitter and TOPCon on n-type Si wafers with the three different doping concentrations. J_0 was extracted according to Ref. [55] including the charge carrier diffusion correction. For Δn below $\sim 3 \times 10^{15}$ cm^{-3}, the data scatters significantly due a strong sensitivity of the J_0 analysis on even a slight scattering of the measured data.

---

[4] The front surface recombination parameter for the perimeter region is $J_{0,front,perimeter} = \sim 5$ fA/cm^2, as determined using dedicated symmetrically processed lifetime test structures, as described below.

Table A1

Physical models and main input parameters for the Quokka device simulations.

Parameter	Value	Uncertainty
Bulk properties:		
Wafer thickness W	variable	$\pm$ 5 µm
Base resistivity ρ_b	variable	$\pm$ 10%
Auger recombination	Ref. [43]	–
Radiative recombination	Ref. [58]	–
Mobility	Ref. [59]	–
Intrinsic carrier concentration	Ref. [60]	–
Bandgap narrowing	Ref. [61]	–
Field emitter p^+:		
$R_{\text{sheet},p+}$	300 Ω/sq	$\pm$ 10%
$J_{0e,p+}$	9 fA/cm^2	$\pm$ 10%
Heavily-doped p^{++} emitter:		
$R_{\text{sheet},p++}$	15 Ω/sq	–
Width	10 µm	$\pm$ 10%
$J_{0e,p++,\text{pass}}$	90 fA/cm^2	$\pm$ 10%
$J_{0e,p++,\text{met}}$	300 fA/cm^2	$\pm$ 10%
$\rho_{C,p++}$	0.4 mΩ cm^2	$\pm$ 50%
Front metal grid:		
Finger pitch	833 µm	–
Finger width	11 µm	$\pm$ 10%
Finger shading fraction	70%	$\pm$ 20%
Finger resistance	3.3 Ω/cm	$\pm$ 20%
Width of contact opening	8 µm	–[a]
Rear passivating contact (TOPCon):		
$J_{0,\text{TOPCon}}$	4 fA/cm^2	$\pm$ 20%
$\rho_{C,\text{TOPCon}}$[b]	50 mΩ cm^2	$\pm$ 20%
Parallel resistance R_p	3.5 kΩ cm^2	$\pm$ 40%
Optical model:		
Surface reflectance	measured	
Z model [35] parameters:		
Z_0	30.69	
Z_∞	1.567	
Z_p	1.631	

[a] Uncertainty included in uncertainty of $\rho_{C,p++}$.
[b] Lumped rear contact resistance from the c-Si through the TOPCon to the Ag rear contact.

excess carrier density Δn range between 10^{15} cm^{-3} and 10^{16} cm^{-3}. For properly adapted f_{opt}, a good agreement of both measurements was observed for all samples. Injection-dependent J_0 results are shown in Fig. A1 for the Al$_2$O$_3$ passivated p^+ emitter and TOPCon on n-type Si wafers with the three doping concentrations.

Table A1 gives also uncertainty ranges for the experimental input parameters, which were estimated from several experimental measurements and thus, represent not only a measurement uncertainty but also a variation of the physical quantity from sample to sample. To estimate the lower limit for the accuracy of the simulation results shown in Figs. 3 and 5 based on these experimental uncertainties, the extreme values of each parameter were combined which are expected to decrease the efficiency, and vice versa for the upper limit.

B. Effective lifetime calculation

The effective lifetime of the fabricated solar cells was calculated according to [62]:

$$\frac{1}{\tau_{\text{eff}}} = \frac{1}{\tau_{\text{intr}}} + \frac{1}{\tau_{\text{SRH}}} + \frac{J_{0,\text{total}}}{qWn_{i,\text{eff}}^2}(N_{\text{dop}} + \Delta n) \tag{B.1}$$

with the lifetime related to intrinsic recombination τ_{intr} (Auger and radiative recombination), the total area-weighted surface recombination parameter $J_{0,\text{total}}$, the effective intrinsic charge carrier concentration $n_{i,\text{eff}}$ and the doping concentration N_{dop}, all as specified in Table A1. The lifetime associated with the SRH recombination τ_{SRH} was calculated based on the recombination properties of Fe given in Ref. [38].

References

[1] J. Nakamura, N. Asano, T. Hieda, C. Okamoto, H. Katayama, K. Nakamura, Development of heterojunction back contact Si solar cells, IEEE J. Photovolt. 4 (6) (2014) 1491–1495.

[2] F. Haase, F. Kiefer, J. Krügener, R. Brendel, R. Peibst, IBC solar cells with polycrystalline on oxide (POLO) passivating contacts for both polarities, presented at the 26th Photovoltaic Specialists Conference, Singapore, 2016.

[3] D. Adachi, J.L. Hernández, K. Yamamoto, Impact of carrier recombination on fill factor for large area heterojunction crystalline silicon solar cell with 25.1%

efficiency, Appl. Phys. Lett. 107 (23) (2015) 233506.

[4] F. Feldmann, M. Bivour, C. Reichel, M. Hermle, S.W. Glunz, Passivated rear contacts for high-efficiency n-type Si solar cells providing high interface passivation quality and excellent transport characteristics, Sol. Energy Mater. Sol. Cells 120 (2014) 270–274.

[5] S.W. Glunz, F. Feldmann, A. Richter, M. Bivour, C. Reichel, H. Steinkemper, J. Benick, M. Hermle, The irresistible charm of a simple current flow pattern – 25% with a solar cell featuring a full-area back contact, in: Proceedings of the 31st European Photovoltaic Specialists Conference and Exhibition, Hamburg, Germany, 2015, pp. 259–263.

[6] K. Masuko, M. Shigematsu, T. Hashiguchi, D. Fujishima, M. Kai, N. Yoshimura, T. Yamaguchi, Y. Ichihashi, T. Mishima, N. Matsubara, T. Yamanishi, T. Takahama, M. Taguchi, E. Maruyama, S. Okamoto, Achievement of more than 25% conversion efficiency with crystalline silicon heterojunction solar cell, IEEE J. Photovolt. 4 (6)

(2014) 1433–1435.

[7] D.D. Smith, P. Cousins, S. Westerberg, R. de Jesus-Tabajonda, G. Aniero, Y.-C. Shen, Toward the practical limits of silicon solar cells, IEEE J. Photovolt. 4 (6) (2014) 1465–1469.

[8] K. Yoshikawa, H. Kawasaki, W. Yoshida, T. Irie, K. Konishi, K. Nakano, T. Uto, D. Adachi, M. Kanematsu, H. Uzu, K. Yamamoto, Silicon heterojunction solar cell with interdigitated back contacts for a photoconversion efficiency over 26%, Nat. Energy 2 (2017) 17032.

[9] J. Bullock, Y. Wan, M. Hettick, J. Geissbuhler, A.J. Ong, D. Kiriya, D. Yan, T. Allen, J. Peng, X. Zhang, C.M. Sutter-Fella, S.D. Wolf, C. Ballif, A. Cuevas, A. Javey, Survey of dopant-free carrier-selective contacts for silicon solar cells, in: Proceedings of the 43rd IEEE Photovoltaic Specialists Conference, Portland, OR, USA, 2016, pp. 210–214.

[10] M. Hermle, Passivated contacts, in: A. Reinders, P. Verlinden, W. van Sark, A. Freundlich (Eds.), Photovoltaic Solar Energy, John Wiley & Sons, Ltd, Chichester, UK, 2016, pp. 125–135.

[11] M. Taguchi, A. Yano, S. Tohoda, K. Matsuyama, Y. Nakamura, T. Nishiwaki, K. Fujita, E. Maruyama, 24.7% record efficiency HIT solar cell on thin silicon wafer, IEEE J. Photovolt. 4 (1) (2014) 96–99.

[12] A. Richter, M. Hermle, S.W. Glunz, Reassessment of the limiting efficiency for crystalline silicon solar cells, IEEE J. Photovolt. 3 (4) (2013) 1184–1191.

[13] J.Y. Gan, R.M. Swanson, Polysilicon emitters for silicon concentrator solar cells, in: Proceedings of the 21st IEEE Photovoltaic Specialists Conference, Kissimmee, USA, 1990, pp. 245–250.

[14] U. Römer, R. Peibst, T. Ohrdes, B. Lim, J. Krügener, E. Bugiel, T. Wietler, R. Brendel, Recombination behavior and contact resistance of n^+ and p^+ poly-crystalline Si/ mono-crystalline Si junctions, Sol. Energy Mater. Sol. Cells 131 (2014) 85–91.

[15] Y. Kwark, R.A. Sinton, R.M. Swanson, Low J0 contact structures using sipos and polysilicon films, in: Proceedings of the 20th IEEE Photovoltaic Specialists Conference, Las Vegas, USA, 1988, pp. 787–792.

[16] E. Yablonovitch, T. Gmitter, R.M. Swanson, Y.H. Kwark, A 720 mV open circuit voltage SiO$_x$:c-Si:Sio$_x$ double heterostructure solar cell, Appl. Phys. Lett. 47 (11) (1985) 1211–1213.

[17] M.K. Stodolny, M. Lenes, Y. Wu, G. Janssen, I.G. Romijn, J. Luchies, L.J. Geerligs, n-Type polysilicon passivating contact for industrial bifacial n-type solar cells, Sol. Energy Mater. Sol. Cells 158 (2016) 24–28.

[18] Y. Tao, V. Upadhyaya, C.-W. Chen, A. Payne, E.L. Chang, A. Upadhyaya, A. Rohatgi, Large area tunnel oxide passivated rear contact n-type Si solar cells with 21.2% efficiency, Prog. Photovolt.: Res. Appl. 24 (6) (2016) 830–835.

[19] A. Moldovan, F. Feldmann, M. Zimmer, J. Rentsch, J. Benick, M. Hermle, Tunnel oxide passivated carrier-selective contacts based on ultra thin SiO$_2$ layers, Sol. Energy Mater. Sol. Cells (2015).

[20] M. Rienacker, M. Bossmeyer, A. Merkle, U. Romer, F. Haase, J. Krugener, R. Brendel, R. Peibst, Junction resistivity of carrier-selective polysilicon on oxide junctions and its impact on solar cell performance, IEEE J. Photovolt. 7 (1) (2017) 11–18.

[21] Y. Tao, E.L. Chang, A. Upadhyaya, B. Roundaville, Y.-.W. Ok, K. Madani, C.-.W. Chen, K. Tate, V. Upadhyaya, F. Zimbardi, J. Keane, A. Payne, A. Rohatgi, 730 mV implied Voc enabled by tunnel oxide passivated contact with PECVD grown and crystallized n$^+$ polycrystalline Si, in: Proceedings of the 42nd IEEE Photovoltaic Specialists Conference, New Orleans, LA, 2015, pp. 1–5.

[22] M. Hermle, F. Feldmann, J. Eisenlohr, J. Benick, A. Richter, B. Lee, P. Stradins, A. Rohatgi, S.W. Glunz, Approaching efficiencies above 25% with both sides-contacted silicon solar cells, in: Proceedings of the 42nd IEEE Photovoltaic Specialists Conference, New Orleans, LA, 2015.

[23] J. Benick, B. Hoex, M.C.M. van de Sanden, W.M.M Kessels, O. Schultz, S.W. Glunz, High efficiency n-type Si solar cells on Al$_2$O$_3$-passivated boron emitters, Appl. Phys. Lett. 92 (25) (2008) 253504.

[24] B. Hoex, J. Schmidt, R. Bock, P.P. Altermatt, M.C.M. van de Sanden, W.M.M. Kessels, Excellent passivation of highly doped p-type Si surfaces by the negative-charge-dielectric Al$_2$O$_3$, Appl. Phys. Lett. 91 (11) (2007) 112107.

[25] A. Richter, J. Benick, M. Hermle, Boron emitter passivation with Al$_2$O$_3$ and Al$_2$O$_3$/ SiN$_x$ stacks using ALD Al$_2$O$_3$, IEEE J. Photovolt. 3 (1) (2013) 236–245.

[26] H. Steinkemper, M. Hermle, S.W. Glunz, Comprehensive simulation study of industrially relevant silicon solar cell architectures for an optimal material parameter choice, Prog. Photovolt.: Res. Appl. 24 (10) (2016) 1319–1331.

[27] F. Feldmann, M. Simon, M. Bivour, C. Reichel, M. Hermle, S.W. Glunz, Efficient carrier-selective p- and n-contacts for Si solar cells, Sol. Energy Mater. Sol. Cells 131 (2014) 100–104.

[28] M. Kerr, A. Cuevas, Generalized analysis of the illumination intensity vs. open-circuit voltage of solar cells, Sol. Energy 76 (1–3) (2004) 263–267.

[29] R.A. Sinton, A. Cuevas, A quasi-steady-state open-circuit voltage method for solar cell characterization, in: Proceedings of 16st European Photovoltaic Specialists Conference and Exhibition, Glasgow, 2000, pp. 1152–1155.

[30] D. Pysch, A. Mette, S.W. Glunz, A review and comparison of different methods to determine the series resistance of solar cells, Sol. Energy Mater. Sol. Cells 91 (18) (2007) 1698–1706.

[31] M. Wolf, H. Rauschenbach, Series resistance effects on solar cell measurements, Adv. Energy Convers. 3 (2) (1963) 455–479.

[32] A. Fell, A free and fast three-dimensional/two-dimensional solar cell simulator featuring conductive boundary and quasi-neutrality approximations, IEEE Trans.

Electron Devices 60 (2) (2013) 733–738.

[33] A. Fell, M.C. Schubert, S.W. Glunz, The concept of skins for (silicon) solar cell modelling, Sol. Energy Mater. Sol. Cells (Silicon PV) (submitted for publication), 2017, doi: 10.1016/j.solmat.2017.05.012.

[34] R. Brendel, Modeling solar cells with the dopant-diffused layers treated as conductive boundaries, Prog. Photovolt.: Res. Appl. 20 (1) (2012) 31–43.

[35] A. Fell, K.R. McIntosh, K.C. Fong, Simplified device simulation of silicon solar cells using a lumped parameter optical model, IEEE J. Photovolt. 6 (3) (2016) 611–616.

[36] R.N. Hall, Electron-hole recombination in germanium, Phys. Rev. 87 (2) (1952) 387.

[37] W. Shockley, W. Read, Statistics of the recombinations of holes and electrons, Phys. Rev. 87 (5) (1952) 835–842.

[38] A.A. Istratov, H. Hieslmair, E.R. Weber, Iron and its complexes in silicon, Appl. Phys. A 69 (1) (1999) 13–44.

[39] D. Macdonald, A. Cuevas, Reduced fill factors in multicrystalline silicon solar cells due to injection-level dependent bulk recombination lifetimes, Prog. Photovolt.: Res. Appl. 8 (4) (2000) 363–375.

[40] M. Reusch, M. Bivour, M. Hermle, S.W. Glunz, Fill factor limitation of silicon heterojunction solar cells by junction recombination, Energy Procedia 38 (2013) 297–304.

[41] P.P. Altermatt, G. Heiser, M.A. Green, Numerical quantification and minimization of perimeter losses in high-efficiency silicon solar cells, Prog. Photovolt. 4 (5) (1996) 355–367.

[42] K.C. Fong, M. Padilla, A. Fell, E. Franklin, K.R. McIntosh, T.C. Kho, A.W. Blakers, Y. Nebel-Jacobsen, S.R. Surve, Perimeter recombination characterization by luminescence imaging, IEEE J. Photovolt. 6 (1) (2016) 244–251.

[43] A. Richter, S.W. Glunz, F. Werner, J. Schmidt, A. Cuevas, Improved quantitative description of Auger recombination in crystalline silicon, Phys. Rev. B 86 (16) (2012) 165202.

[44] K. Graff, Metal Impurities in Silicon-Device Fabrication, 2nd ed., Springer, Berlin, 2000.

[45] D. Macdonald, A. Cuevas, K. McIntosh, L. Barbosa, D. de Ceuster, Impact of Cr, Fe, Ni, Ti and W surface contamination on diffused and oxidised n-type crystalline silicon wafers, in: Proceedings of the 20th European Photovoltaic Specialists Conference and Exhibition, Barcelona, Spain, 2005, pp. 627–630.

[46] D. Macdonald, L.J. Geerligs, Recombination activity of interstitial iron and other transition metal point defects in p- and n-type crystalline silicon, Appl. Phys. Lett. 85 (18) (2004) 4061–4063.

[47] G. Coletti, P.C.P. Bronsveld, G. Hahn, W. Warta, D. Macdonald, B. Ceccaroli, K. Wambach, N. Le Quang, J.M. Fernandez, Impact of metal contamination in silicon solar cells, Adv. Funct. Mater 21 (2011), pp. 879–890.

[48] M.D. Abbott, D. Poplavskyy, G. Scardera, D. Inns, F. Lemmi, K.R. McIntosh, S.C. Baker-Finch, Iron contamination in silicon solar cell production environments, in: Proceedings of the 40th IEEE Photovoltaic Specialists Conference, Denver, CO, USA, 2014, pp. 3479–3484.

[49] E. Yablonovitch, D. Allara, C. Chang, T. Gmitter, T. Bright, Unusually low surface-recombination velocity on silicon and germanium surfaces, Phys. Rev. Lett. 57 (2) (1986) 249–252.

[50] S. Rein, Lifetime Spectroscopy: A Method Of Defect Characterization In Silicon For Photovoltaic Applications, 1st ed., Springer, Berlin, New York, 2005.

[51] A. Richter, et al., (submitted for publication), 2017.

[52] R. Brendel, S. Dreissigacker, N.-P. Harder, P.P. Altermatt, Theory of analyzing free energy losses in solar cells, Appl. Phys. Lett. 93 (17) (2008) 173503.

[53] M.A. Green, K. Emery, Y. Hishikawa, W. Warta, E.D. Dunlop, D.H. Levi, A.W.Y. Ho-Baillie, Solar cell efficiency tables (version 49), Prog. Photovolt.: Res. Appl. 25 (1) (2017) 3–13.

[54] D.E. Kane, R.M. Swanson, Measurement of the emitter saturation current by a contactless photoconductivity decay method (silicon solar cells), in: Proceedings of the 18th IEEE Photovoltaic Specialists Conference, Las Vegas, 1985, pp. 578–583.

[55] A. Kimmerle, J. Greulich, A. Wolf, Carrier-diffusion corrected J0-analysis of charge carrier lifetime measurements for increased consistency, Sol. Energy Mater. Sol. Cells 142 (2015) 116–122.

[56] R.A. Sinton, A. Cuevas, Contactless determination of current–voltage characteristics and minority-carrier lifetimes in semiconductors from quasi-steady-state photo-conductance data, Appl. Phys. Lett. 69 (17) (1996) 2510–2512.

[57] H. Nagel, C. Berge, A.G. Aberle, Generalized analysis of quasi-steady-state and quasi-transient measurements of carrier lifetimes in semiconductors, J. Appl. Phys. 86 (11) (1999) 6218–6221.

[58] H.T. Nguyen, F.E. Rougieux, B. Mitchell, D. Macdonald, Temperature dependence of the band-band absorption coefficient in crystalline silicon from photolumines-cence, J. Appl. Phys. 115 (4) (2014) 43710.

[59] D.B.M. Klaassen, A unified mobility model for device simulation: I. Model equations and concentration dependence, Solid State Electron. 35 (7) (1992) 953–959.

[60] R. Couderc, M. Amara, M. Lemiti, Reassessment of the intrinsic carrier density temperature dependence in crystalline silicon, J. Appl. Phys. 115 (9) (2014) 93705.

[61] A. Schenk, Finite-temperature full random-phase approximation model of band gap narrowing for silicon device simulation, J. Appl. Phys. 84 (7) (1998) 3684–3695.

[62] H. Mäckel, K. Varner, On the determination of the emitter saturation current density from lifetime measurements of silicon devices, Prog. Photovolt.: Res. Appl. 21 (5) (2013) 850–866.